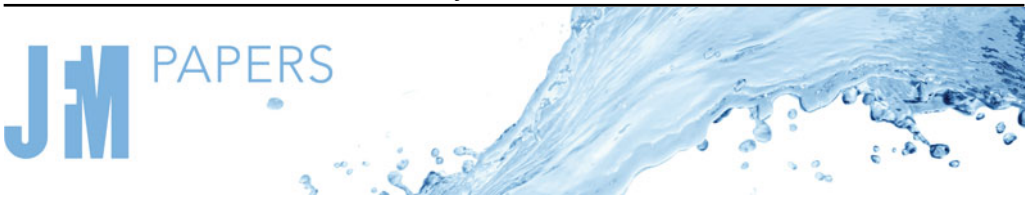
J. Fluid Mech. (2026), *vol.* 1034, A1, doi:10.1017/jfm.2026.11481



Uni/bifractality of velocity circulation in wall-parallel concentric shells of turbulent pipe flow

Baofang Song[1] **and Duo Xu**[2,3]

[1]State Key Laboratory for Turbulence and Complex Systems, Department of Aeronautics and Astronautics, School of Mechanics and Engineering Science, Peking University, Beijing 100871, PR China

[2]The State Key Laboratory of Nonlinear Mechanics, Institute of Mechanics, Chinese Academy of Sciences, No. 15 Beisihuanxi Road, 100190, Beijing, PR China

[3]School of Engineering Science, University of Chinese Academy of Sciences, No.1 Yanqihu East Rd, Beijing, 100049, PR China

Corresponding author: Duo Xu, duo.xu@imech.ac.cn

(Received 29 October 2025; revised 25 March 2026; accepted 26 March 2026)

Turbulent pipe flow is of substantial importance in practical applications, and it remains challenging to depict the characteristic complex multiscale dynamics by a unified theoretical framework, hindered by its inherent intermittency. Inspired by a recent study of velocity circulation in turbulent channel flows from Duan, Chen & Sreenivasan (2025 *J. Fluid Mech.*, vol. 1009, p. R4), in this study, we investigate the statistical characteristics of velocity circulation (or equally the area integral of wall-normal vorticity) over rectangular loops in concentric cylindrical shells, parallel to the pipe wall. The statistics are implemented using direct numerical simulation data at friction Reynolds numbers of $Re_\tau = 1057$ and 2000. Close to the pipe wall, the circulation in the inertial range resides on space-filling unifractal sets, with the Hölder exponent smaller than Kolmogorov's 4/3. Away from the pipe wall, the circulation displays bifractal characteristics and the Hölder exponents for high moment orders are very close to those reported in channel flows and homogeneous isotropic turbulence. The circulation statistics are only dependent on the area enclosed by the loops, and are invariant to the loop aspect ratio, once both edge lengths of the loops are in the inertial range.

Key words: intermittency, pipe flow, turbulence theory

1. Introduction

Along with the randomness in turbulence, evidencing its universal features at small scales has been a long-lasting task. Such efforts have been most often attempted through a

© The Author(s), 2026. Published by Cambridge University Press.

https://doi.org/10.1017/jfm.2026.11481 Published online by Cambridge University Press

diagnostic tool, the so-called structure function of the velocity, $\langle|\delta u_r|^p\rangle$, where δu_r is the velocity increment over a distance r, p is the moment order and $\langle\cdot\rangle$ denotes an ensemble average operation. The scaling law in the structure function, $\langle|\delta u_r|^p\rangle \propto r^{\chi_p}$ with scaling exponent χ_p, can characterise the energy cascade among scales, and the pioneering work of Kolmogorov (1941) predicted that $\chi_p = p/3$ in the inertial range, a range of scales far from both of the forcing and the dissipation scales. However, later studies have shown that the structure functions in the inertial range are multifractal (Frisch 1995), given that the scaling exponent is a nonlinear function of the moment order (e.g. She & Leveque 1994; Sreenivasan & Yakhot 2021). The difficulty of multifractality makes itself challenging to understand analytically and therefore motivates alternative theoretical frameworks to describe the turbulence. Migdal (1994, 1995, 2023) proposed a statistical framework of velocity circulation Γ_A around closed Eulerian loops, arguing that the tails of the probability density function (i.e. $P(\Gamma_A)$) depend only on the minimal area enclosed by the Eulerian loop, regardless of its shape, once the loop is entirely in the inertial range. This is the so-called the area rule. The velocity circulation that he considered is

$$\Gamma_A = \oint_C \boldsymbol{u}' \cdot \mathrm{d}\boldsymbol{l} = \iint_A \boldsymbol{\omega} \cdot \boldsymbol{n}\mathrm{d}A, \tag{1.1}$$

where $\boldsymbol{u}'$ is the fluctuating velocity, C is the boundary of a loop with area A, $\mathrm{d}\boldsymbol{l}$ is an elemental length along C, $\boldsymbol{\omega} = \boldsymbol{\nabla} \times \boldsymbol{u}'$ is the corresponding vorticity and $\boldsymbol{n}\mathrm{d}A$ is an elemental area of A in the direction of the unit normal $\boldsymbol{n}$. Correspondingly, in Kolmogorov's (1941) framework, it follows that $|\Gamma_A|^p \propto A^{\zeta_p} \propto r^{\xi_p}$ for $p = 2$, where $\xi_p = 4p/3$ and $\zeta_p = \xi_p/2$. It was shown that this relationship closely holds for $p = 3$ also (Iyer, Sreenivasan & Yeung 2019). However, no evidence has been reported for its applicability to higher moment orders. It should be noted that Migdal's proposition is only approximately correct because recent results of Iyer, Bharadwaj & Sreenivasan (2021) showed a noticeable, although small within a few per cent, loop-shape dependence of the probability density function (PDF) of circulation moments, and a proper normalisation of the PDF by an internal variable (e.g. some moments) is needed to make the circulation PDF more closely shape-independent.

This framework was explored in several early attempts (Umeki 1993; Sreenivasan, Juneja & Suri 1995; Cao, Chen & Sreenivasan 1996; Benzi *et al.* 1997; Zhou, Sun & Xia 2008). The verification of the area rule is hampered by the modest size of the inertial range at moderate Reynolds numbers. Recently, Iyer *et al.* (2019) has shown that the scaling exponent ξ_p in moments of velocity circulation is bifractal in a high-Reynolds-number homogeneous isotropic turbulence (HIT). This bifractality shows considerably more simplicity in the velocity circulations than the multifractality in the velocity structure functions. The bifractality in the velocity circulation was later reported in quantum turbulence (Müller *et al.* 2021; Polanco, Müller & Krstulovic 2021), quasi-two-dimensional turbulence experiments (Zhu, Xie & Xia 2023), where the flows have no mean shear. It should be noted that the above mentioned bifractality is a close approximation instead of an exact relationship, as also pointed out by Apolinário *et al.* (2020) and Moriconi (2021). With a mean strain, in turbulent flow passing through a contraction, approximate bifractality of circulation is also evidenced (Mugundhan & Thoroddsen 2023; Alhareth *et al.* 2024). In a very recent study of turbulent channel flow, Duan, Chen & Sreenivasan (2025) have shown that, at parallel planes close to the wall, the scaling exponent ξ_p is monofractal with no intercepts, implying that the velocity circulation resides on space-filling unifractal sets; at the parallel planes far away from the wall, ξ_p is bifractal, in analogy to the works of Iyer *et al.* (2019), Müller *et al.* (2021), Polanco *et al.* (2021) and Zhu *et al.* (2023). This suggests the possibility of bifractality in general

https://doi.org/10.1017/jfm.2026.11481 Published online by Cambridge University Press

Re_τ	Re_b	L	Δr^+_{min}	Δr^+_{max}	$R^+\Delta\theta$	Δz^+	N	M	K
1057	40 000	10	0.07	3.5	8.6	13.8	320	768	768
2000	83 000	5	0.06	3.8	6.5	10.2	512	1920	976

Table 1. Parameters and grid resolutions used for the simulations. Here, Δr^+_{min} is the number of non-uniform finite-difference grid points in radial direction, and M and K are the total number of Fourier modes (also the number of uniform grid points) in the azimuthal and axial directions, respectively, before dealiasing.

wall-bounded shear flows, a more common circumstance in practice. This motivates our investigation in this study. In addition, these studies took the statistics in flat planes (e.g. Iyer *et al.* 2019; Zhu *et al.* 2023; Duan *et al.* 2025) or perpendicular connected planes (Iyer *et al.* 2021). Here, we examine the statistics of velocity circulation in turbulent pipe flows, which have curved walls, and the statistics are performed on the wall-parallel planes (i.e. concentric cylindrical shells). Given that pipe flows are prototypes of a variety of flows and have substantial practical applications in engineering, simplicity in modelling this intermittent turbulence would benefit the related problems.

The method of direct numerical simulation is briefly introduced in § 2. The statistical results of the circulation are shown in § 3. The conclusions are drawn in § 4.

2. Method

Incompressible Navier–Stokes equations are solved in cylindrical coordinates (r, θ, z) with periodic boundary condition in the axial direction and a no-slip boundary condition on the pipe wall. A Fourier spectral finite-difference code (Openpipeflow) is used for the simulation (Willis 2017), which has been used for studies of transition to turbulence (e.g. Willis & Kerswell 2009; Avila, Willis & Hof 2010; Xu & Avila 2018; Chen, Xu & Song 2022) and fully developed turbulence with very large friction Reynolds numbers (Yao *et al.* 2023). For this study, two friction Reynolds numbers of $Re_\tau = u_\tau R/\nu = 1057$ ($Re_b = U_{max}R/\nu = 40\,000$) and $Re_\tau = 2000$ ($Re_b = 83\,000$) are considered, where $u_\tau = \sqrt{\tau_w/\rho}$ is the friction velocity, R the pipe radius and U_{max} the maximum velocity of the basic laminar flow. Here ν is kinematic viscosity of fluid, τ_w is wall shear stress and ρ is fluid density. The pipe length is selected to be approximately $L^+ = 10\,000$ for both cases, an order of magnitude larger than the size of near-wall velocity streaks, where a length with a superscript '+' is normalised by ν/u_τ (wall units). Note that L^+ is related to the length in outer units (i.e. in units of pipe radius), L, by the relationship $L^+ = Re_\tau L$. The grid resolutions for the simulations are listed in table 1. The Kolmogorov length scale is calculated as $\eta = (\nu^3/\langle\epsilon\rangle)^{1/4}$, where $\epsilon = 2\nu\langle s_{ij}s_{ij}\rangle$ is the dissipation rate of the turbulent kinetic energy, $s_{ij} = 1/2(\partial u_i'/\partial x_j + \partial u_j'/\partial x_i)$ is the fluctuating strain rate and $\langle\cdot\rangle$ denotes ensemble average. Note that η depends on the wall distance $y = R - r$ and should therefore be calculated using the local ϵ. The wall distance in wall units will be denoted as $y^+ = (y/R)Re_\tau$, giving $y^+ = Re_\tau$ at the pipe centre.

Figure 1(*a*,*b*) shows the mean velocity profile U^+ and its wall-normal derivative $\mathrm{d}U^+/\mathrm{d}y^+$ for $Re_\tau = 2000$. The vertical dotted lines show the wall-normal positions considered in the following circulation analysis, which are $y^+ = 10, 20, 40$, which are in the sublayer and buffer layer, and $0.2Re_\tau \sim 0.9Re_\tau$, which are in the outer region. From the plot of $\mathrm{d}U^+/\mathrm{d}y^+$, it can be seen that shear is strong in the inner region whereas it is small in the outer region (see figure 1*b*). In order to ensure homogeneity of the flow field within the integration path, data in concentric cylindrical shells are considered for the calculation of the circulation (illustrated in figure 1*c*). For simplicity, rectangular loops

https://doi.org/10.1017/jfm.2026.11481 Published online by Cambridge University Press

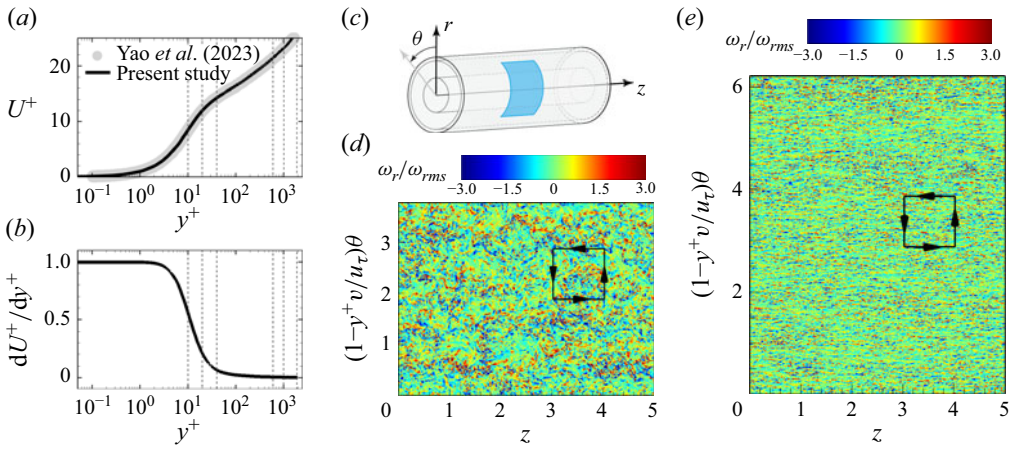


Figure 1. (*a*) Mean velocity profile and (*b*) mean shear profile for $Re_\tau = 2000$. (*c*) Sketch of the computational domain, where the cylindrical coordinate system is set and two cylindrical shells are illustrated. The blue shade shows a rectangular loop and the enclosed area in a cylindrical shell, over which circulation is calculated. Contours of vorticity $\omega_r/\omega_{r,rms}$ in the shells at $y^+ = 0.4Re_\tau$ (*d*) and $y^+ = 20$ (*e*). The two shells are unfolded onto flat planes with streamwise coordinate z being the horizontal axis and azimuthal coordinate $r\theta = (1 - y^+v/u_\tau)\theta$ being the vertical axis.

with the same enclosed area A as in a cylindrical shell are selected as the integration paths, with which the scaling of the circulation moments with the area A and the influence of the aspect ratio of the area on the statistics can be investigated. Figure 1(*d*,*e*) illustrates the wall-normal vorticity ω_r on the cylindrical shells at $0.4Re_\tau$ and $y^+ = 20$ as examples and an integration loop (the yellow rectangle). It can be seen that the flow at $y^+ = 20$, which is in the buffer layer, shows streamwise elongated structures, whereas the flow at $y^+ = 0.4Re_\tau$ appears to be more isotropic within the shell.

3. Results

3.1. *Moments of circulation*

In a selected cylindrical shell, circulation is calculated over rectangular loops, as sketched in figure 1(*c–e*). For simplicity, the sides of loops are parallel to either the streamwise or azimuthal direction. By shifting the loop on the grids in the shell and by using data from 20 snapshots, a sample of the circulation can be constructed. Depending on the step size of the shift, different sample sizes can be obtained. For example, the maximal sample size of the $Re_\tau = 2000$ case is approximately 8.4×10^7 with our de-aliased grid. We tested different sample sizes and found no significant effect on the statistics. In the following, we only show the statistics with the maximal sample size.

The second-order moment $\langle|\Gamma_A|^2\rangle$ is first calculated with a fixed aspect ratio (AR) of one and shown as a function of A/η^2 in figure 2. The inner region, i.e. the buffer layer and sublayer, and the outer layer of $y^+ > 0.1Re_\tau$ are shown separately. It is found that $\langle|\Gamma_A|^2\rangle \propto A^{\zeta_p}$ in certain ranges of A. In the outer region, where shear is small (figure 1*b*), data from all three considered y^+ collapse and approximately follow a $A^{4/3}$ scaling over at least one decade of A/η^2, between 10^3 and 10^4 (see figure 2*b*). This power-law scaling can be more quantitatively evidenced by the appearance of a plateau region in the plot of $d\log[\langle|\Gamma_A|^2\rangle]/d\log[A/\eta^2]$, as shown in figure 2(*d*). The power-law scaling agrees with the Kolmogorov theory for HIT derived from the Stokes theorem that associates the circulation statistics with the structure function statistics (e.g. Migdal

https://doi.org/10.1017/jfm.2026.11481 Published online by Cambridge University Press

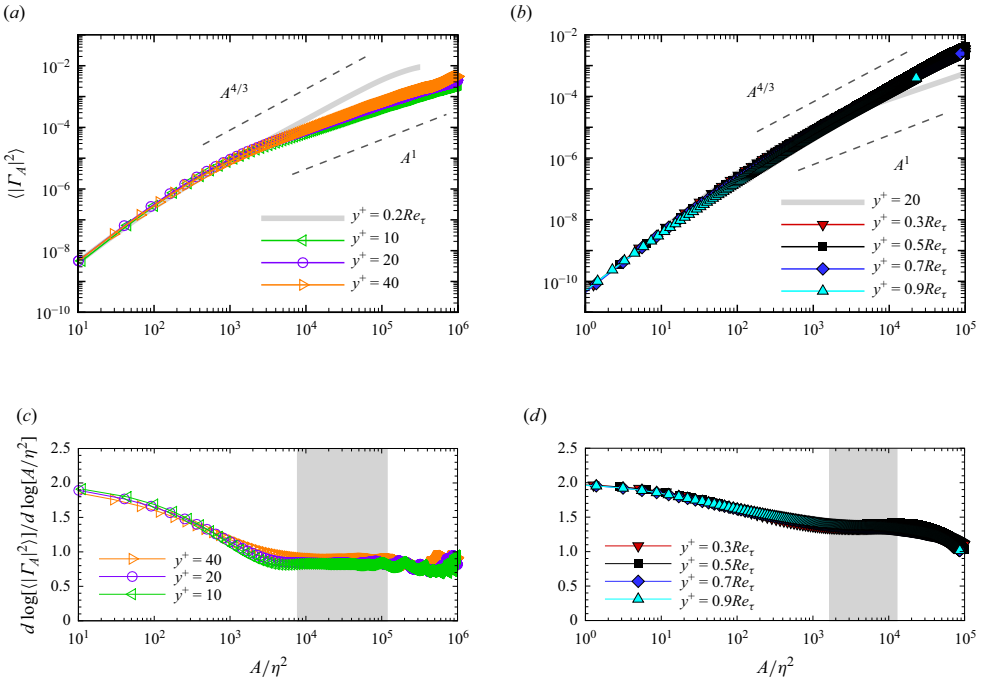


Figure 2. Second-order circulation moments $\langle|\Gamma_A|^2\rangle$ at $Re_\tau = 2000$ as a function of the loop area A/η^2: (*a*) $y^+ = 10, 20, 40$ in the inner region; (*b*) $y^+ = 0.3Re_\tau \sim 0.9Re_\tau$ in the outer region. To contrast the scalings in these two regions, $y^+ = 0.2Re_\tau$ from the outer region is shown as a bold grey line in panel (*a*), and $y^+ = 20$ from the inner region is shown as a bold grey line in panel (*b*). The corresponding plots of $d\log[\langle|\Gamma_A|^2\rangle]/d\log[A/\eta^2]$ are shown in panels (*c*) and (*d*). For reference, in outer units, Kolmogorov length scales are $\eta = 8.13\times10^{-4}$, 8.54×10^{-4}, 9.99×10^{-4}, 1.83×10^{-3}, 2.02×10^{-3}, 2.18×10^{-3}, 2.30×10^{-3}, 2.55×10^{-3} and 2.88×10^{-3} at $y^+ = 10$, 20, 40, $0.2Re_\tau$, $0.3Re_\tau$, $0.4Re_\tau$, $0.5Re_\tau$, $0.7Re_\tau$ and $0.9Re_\tau$, respectively.

1994; Iyer *et al.* 2019). However, Iyer *et al.* (2019) reported that the power index from Kolmogorov's theory is only close to but not identical to the actual value from the HIT data (4/3 vs. 1.367). In the inner region where shear is strong (figure 1*b*), data also exhibit a power-law scaling in a certain area range that is slightly shifted toward larger A and wider compared with the outer region, see figure 2(*a*,*c*). In comparison, the scaling exponent appears to be smaller than 1 and shows a decreasing trend when approaching the pipe wall. This deviation of the exponent from 4/3 is presumably attributed to the deviation from isotropy of the flow structure in the inner region due to the strong shear.

The higher-order moments $\langle|\Gamma_A|^p\rangle$ are also calculated and shown in figure 3. Similarly, for both inner and outer regions, a power-law scaling range can be approximately observed for each moment, $\langle|\Gamma_A|^p\rangle \propto A^{\xi_p} \propto r^{\xi_p}$, and the scaling exponent increases as the order p increases. The scaling range in the outer region seems to be slightly shifted toward smaller A (i.e. $10^3 < A/\eta^2 < 10^4$, approximately) compared with that in the inner region (i.e. $10^4 < A/\eta^2 < 10^5$, approximately), consistent with the observation in figure 2.

3.2. *Scaling exponent and fractality*

The exponent ξ_p as a function of the order p can be used to investigate the fractal property of the flow field. Our data show that, in the inner region, at $y^+ = 10$, 20 and 40, each data set for ξ_p can be fitted well by a straight line through the origin (figure 4*a*), although the

https://doi.org/10.1017/jfm.2026.11481 Published online by Cambridge University Press

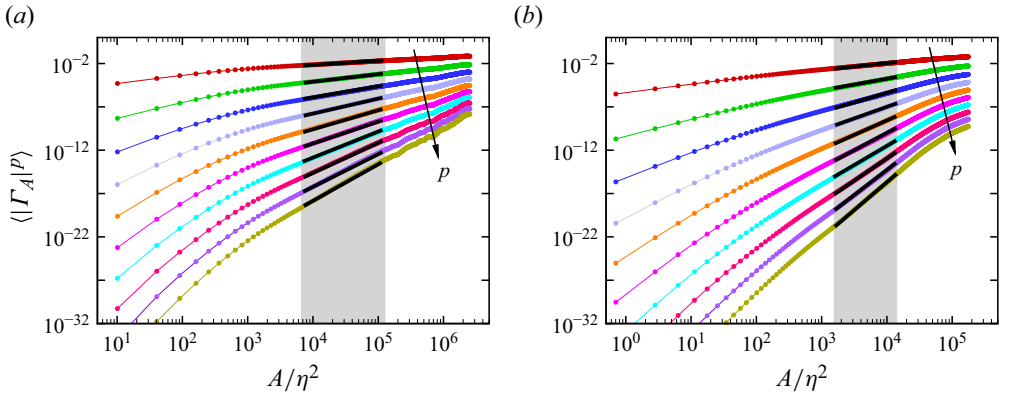


Figure 3. Circulation moments with integer order $1 \leqslant p \leqslant 10$: (*a*) $y^+ = 20$; (*b*) $y^+ = 0.3Re_\tau$. The black solid lines indicate the scaling for fitting for the scaling exponents. $Re_\tau = 2000$.

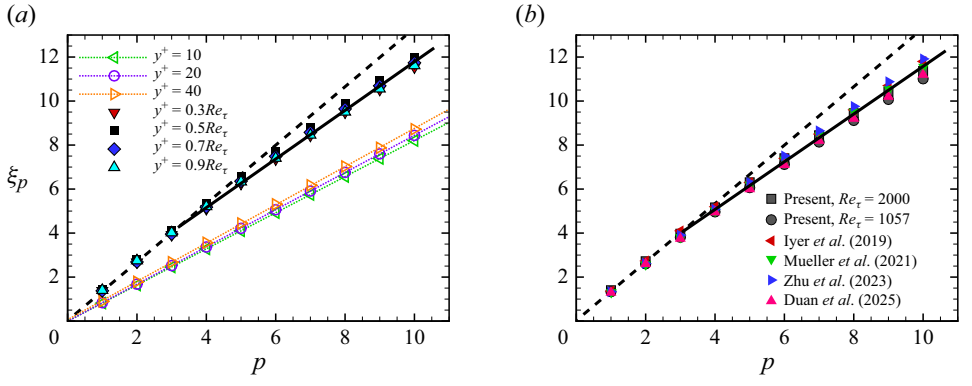


Figure 4. (*a*) The scaling exponent ξ_p as a function of the moment order p for $Re_\tau = 2000$. The black dashed line is the Kolmogorov theory, $\xi_p = 4p/3$. The black solid line indicates the mono-fractal model for $0.2Re_\tau \leqslant y^+ \leqslant 0.4Re_\tau$, $\xi_p = 1.09p + 0.87$. The dotted lines mark unifractality below the log layer. (*b*) The scaling exponent ξ_p as a function of the moment order p with the data of three-dimensional HIT (Iyer *et al.* 2019), quantum turbulence (Müller *et al.* 2021), quasi-two-dimensional turbulence (Zhu *et al.* 2023), channel flow (Duan *et al.* 2025) and the present pipe flow ($Re_\tau = 1057$ and $Re_\tau = 2000$).

slope of the line varies slightly with the wall distance. In contrast, in the outer region, the data cannot be fitted by a single straight line but require two. One for the low orders $p \leqslant 3$ through the origin and the other for higher orders with a non-zero intercept (figure 4*b*). By fitting ξ_p with

$$\xi_p = hp + (2 - D), \tag{3.1}$$

the Hölder exponent h, which represents the degree of singularity (Frisch 1995), and the corresponding fractal dimension D can be obtained in the outer region. The results indicate that ξ_p for different y^+ in the outer region collapses approximately and can therefore be fitted by a general relationship. For low orders of $p \lesssim 3$, the Kolmogorov theory $\xi_p = 4p/3$ fits the data reasonably well and for higher orders, the relationship $\xi_p = 1.09p + 0.87$ fits the data approximately, which gives the fractal dimension $D = 1.13$. The fit $h \approx 1.09$ is close to the observations in the studies of Iyer *et al.* (2019), Iyer *et al.* (2021), Müller *et al.* (2021), Zhu *et al.* (2023) and Duan *et al.* (2025). Notably, the scaling

https://doi.org/10.1017/jfm.2026.11481 Published online by Cambridge University Press

exponent $\zeta_p = \xi_p/2 \approx 0.545$ closely aligns with $h = 1/2$ at high moment orders within the framework of Migdal (1994, 1995, 2023).

These observations reflect the unifractality in the inner region and the bifractal nature in the outer region of the vorticity field. The present results, including that of a lower Re_τ at 1057, are also compared with those from the literature in figure 4(*b*). Overall, a good agreement between the scaling exponent with that of other types of flow, including three-dimensional HIT (Iyer *et al.* 2019), channel flow (Duan *et al.* 2025), quasi-two-dimensional turbulence (Zhu *et al.* 2023) and quantum turbulence (Müller *et al.* 2021). This agreement suggests that the bifractality is a general property of the flow field sufficiently far from the wall. Besides, the Hölder exponent and fractal dimension are also quantitatively close among different flows.

Figure 5 shows the PDF of the circulation Γ_A, normalised by $u_{rms}R$, where u_{rms} is the root mean square of the local streamwise velocity fluctuations. It is observed that the PDF of the inner region appears to be Gaussian approximately, and the PDFs at the selected wall distances nearly collapse with this normalisation (figure 5*a*). In comparison, the PDF of the outer layer deviates significantly from a Gaussian, with the tails being much higher than the Gaussian (figure 5*b*). The deviation can be more quantitatively illustrated by using the flatness (kurtosis), $F(A) = \langle|\Gamma_A|^4\rangle/\langle|\Gamma_A|^2\rangle^2$, which is 3 for a Gaussian distribution and larger/smaller than 3 for broader/narrower distributions. Figure 5(*c*) shows that in the inner region, F is approximately 3 in the scaling range of the circulation moments ($10^3 \lesssim A/\eta^2 \lesssim 10^5$), while it significantly deviates from 3 in the outer region for the scaling range of $10^2 \lesssim A/\eta^2 \lesssim 10^4$, showing a more heavily tailed behaviour. It is also observed that the farther we are from the pipe wall, the larger the deviation from the Gaussian (figure 5*c*). As proposed by Duan *et al.* (2025), viscosity acts against the singularity of the flow field by damping out extreme fluctuations and consequently makes the statistics more Gaussian. Therefore, it can be expected that the closer we are to the pipe centre, the weaker the viscous effects and the more tailed the PDF. This interpretation is consistent with our results.

The no-slip and no-penetration conditions give a more distinct viscous effect close to the wall, but the wall-normal vorticity there does not exhibit a Gaussian PDF, as shown in figure 5(*d*). Nevertheless, in comparison, $P(\omega_r)$ is closer to the Gaussian distribution for $y^+ \lesssim 40$, while $P(\omega_r)$ for $y^+ \gtrsim 0.3Re_\tau$ is more tailed (figure 5*e*), indicating that ω_r is more intermittent there than that close to the wall. This demonstrates that the viscous effect alone is insufficient to give a Gaussian distribution of ω_r for Γ_A with very small area A to exhibit the unifractality shown in figure 4(*a*). With the area integration of ω_r (see (1.1)), the intermittency level reduces as the area of the integration loop increases, indicated by the decrease of $F(A)$ shown in figure 5(*c*), where the reduction rate of the kurtosis $F(A)$ in terms of A is comparable for different y^+. For $y^+ \leqslant 40$, $F(A)$ reaches $F \approx 3$ at around $A/\eta^2 \approx 10^3$ and stays at $F \approx 3$ beyond, given by the low intermittency level of the vorticity. Meanwhile, the inertial range for $y^+ \leqslant 40$ is reached when $10^4 \lesssim A/\eta^2 \lesssim 10^5$ (see figures 2*d* and 3*b*, also indicated by double-headed arrows in figure 5*c*), falling in the range for a nearly Gaussian distribution with $F \approx 3$. This results in the approximate Gaussian distribution of Γ_A in the inertial range close to the wall, and correspondingly the unifractability, implying the necessity of the averaging effect of the area integration. In contrast, for $y^+ \geqslant 0.3Re_\tau$, $F \approx 3$ is reached only at $A/\eta^2 \gtrsim 10^4$, due to the relatively high intermittency level of the vorticity, while the inertial range is $10^3 \lesssim A/\eta^2 \lesssim 10^4$ (see the spanned scales by the double-headed arrows in figure 5*c*). This mismatched ranges of length scales drives Γ_A to deviate from the unifractality. This suggests further that the averaging effect of the area integration is a necessary factor, in addition to the viscous effect, for reaching the unifractality.

https://doi.org/10.1017/jfm.2026.11481 Published online by Cambridge University Press

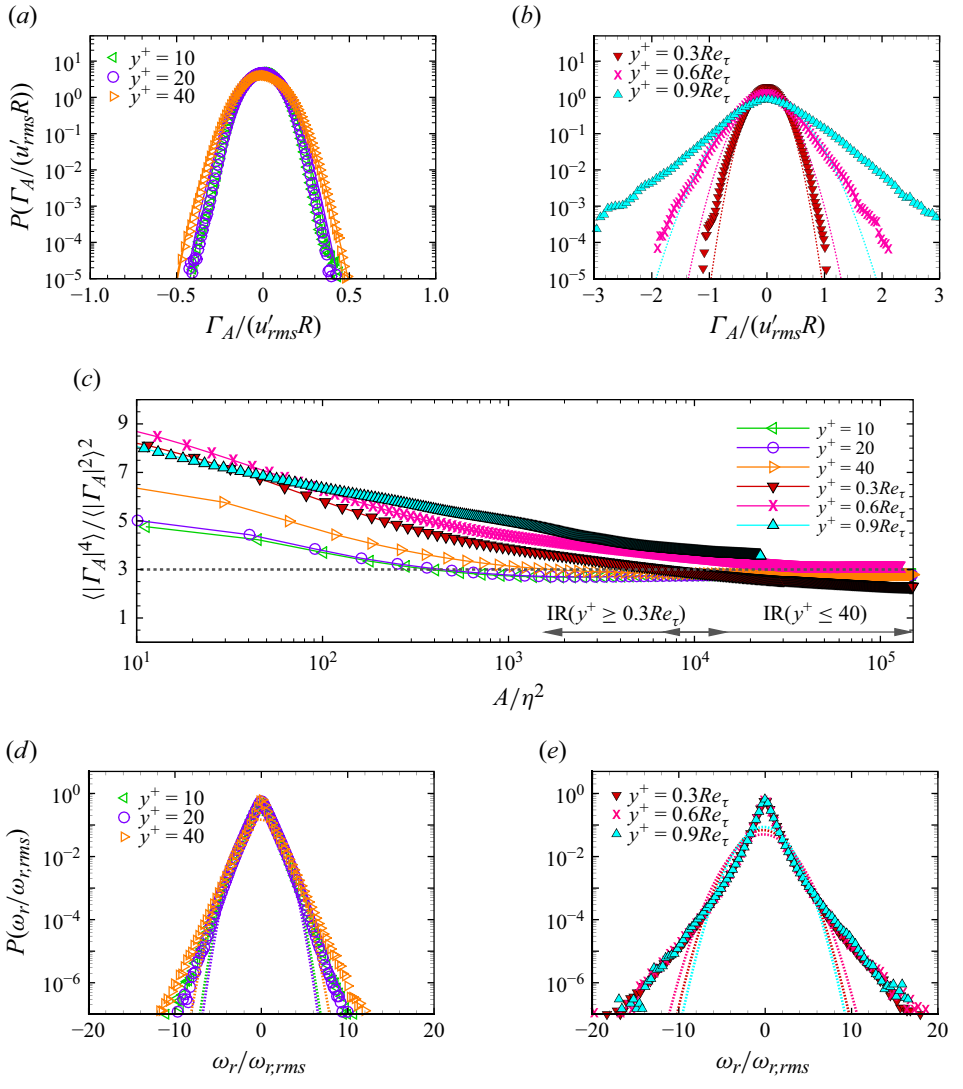


Figure 5. Probability density function P of Γ_A for (*a*) $y^+ = 10$, 20, 40 and (*b*) $y^+ = 0.3Re_\tau$, $0.6Re_\tau$, $0.9Re_\tau$. They are taken with the same loop size of $A/\eta^2 = 5000$. The lines denote respective Gaussian PDFs. (*c*) Circulation flatness $\langle|\Gamma_A|^4\rangle/\langle|\Gamma_A|^2\rangle^2$ at the radial shells as a function of the integration area, where the double-headed arrows indicate the corresponding inertial ranges (IRs). (*d*, *e*) Probability density function P of vorticity ω_r. In (*a*, *b*, *d*, *e*) dotted lines in corresponding colours show fits with a Gaussian. The data are from $Re_\tau = 2000$.

From the perspective of turbulent flow structures, vortical structures root near the wall and have a preferential direction along the streamwise direction (e.g. Adrian 2007; Wu & Moin 2009; Jodai & Elsinga 2016; Marusic & Monty 2019) regardless of specific types, and they are contributed mainly by the streamwise vorticity and secondarily by the wall-normal and azimuthal vorticity components, associated with the no-slip and no-penetration conditions. This helps the wall-normal vorticity to be weakly intermittent, giving unifractality after some area integration, where the area is large enough to cover balanced extreme positive and negative wall-normal vorticities. Differently, away from the wall, the vortical structures lift up to be more perpendicular to the main streamwise

https://doi.org/10.1017/jfm.2026.11481 Published online by Cambridge University Press

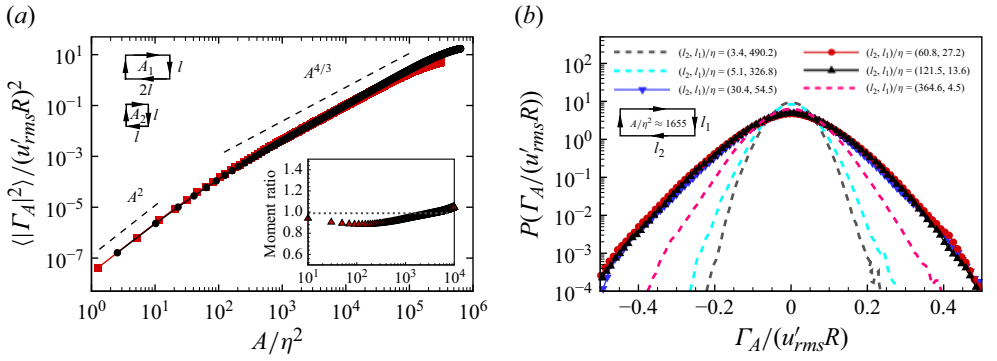


Figure 6. (*a*) Second-order circulation moments as a function of area, where the red squares are for the aspect ratio of 1 : 1 and the black filled circles are for the aspect ratio of 2 : 1. The inset show the moment ratio $\langle\Gamma_{A_2}^2\rangle/\langle\Gamma_{A_1}^2\rangle$ as a function of the area. (*b*) Probability density function of Γ_A with a fixed area $A/\eta^2 \approx 1655$ but with different aspect ratios l_2/l_1. The data are from $y^+ = 0.3Re_\tau$ and $Re_\tau = 2000$.

direction, where the wall-normal vorticity makes a much greater contribution. This possibly makes the wall-normal vorticity statistics display a stronger intermittency, leading to the deviation from unifractality.

So far all results have been obtained with the aspect ratio $AR = 1$ of the integration loop. In the following, the effect of AR on the statistics is discussed. Figure 6(*a*) shows the comparison of $\langle\Gamma_A^2\rangle$ for the aspect ratios of $AR = 2$ and 1. Good agreement between the two can be observed, indicating that, for the considered AR values, the scaling of $\langle\Gamma_A^2\rangle$ is not noticeably dependent on AR. This can be further shown by the ratio between the two moments, $\langle\Gamma_{A_2}^2\rangle/\langle\Gamma_{A_1}^2\rangle$, as shown by the inset in figure 6(*a*). Indeed, in the power-law scaling range of $A/\eta^2 \simeq 10^3 - 10^4$, the ratio is nearly unity. It is also noted from the data that there appears to be a A^2 scaling of $\langle\Gamma_A^2\rangle$ below $A/\eta^2 = 10$, i.e. in the dissipation range, in which the ratio is also nearly 1, indicating an AR independence as well. A broader range of AR is considered to show a full picture. For this study, we fix $A/\eta^2 \approx 1655$ and vary the lengths l_1 and l_2, covering both the dissipation and inertia length scales. As shown in figure 6(*b*), the PDFs of the circulation approximately collapse when both l_1 and l_2 are within the inertial range ($30 \lesssim l/\eta \lesssim 125$, see the filled symbols with solid lines), while it deviates and changes with the specific values of AR otherwise. This observation is consistent with the results of Duan *et al.* (2025) for channel flow, as also evidenced in two-/three-dimensional HIT (Iyer *et al.* 2019; Zhu *et al.* 2023) and quantum turbulence (Müller *et al.* 2021; Polanco *et al.* 2021).

In figure 6 we examined the effect of aspect ratio on the low-order circulation moment, where recently Iyer *et al.* (2021) showed that the validation of area rule may differ, particularly for the high orders. Following Iyer *et al.* (2021), we examine the logarithm of the ratio of successive even-order moments $\ln[\langle\Gamma_A^{2m}\rangle^{1/2m}/\langle\Gamma_A^{2m-2}\rangle^{1/(2m-2)}]$ with varying aspect ratios, where m is an integer and the loop-enclosed area A is fixed. We show two examples in figure 7, one at $y^+ = 40$ (unifractality) in panel (*a*) and the other at $y^+ = 0.3Re_\tau$ (bifractality) in panel (*b*). As the order $2m$ increases, the ratios show better independence of the aspect ratio for both y^+ values. Iyer *et al.* (2021) fit the tails of the circulation PDF using a gamma function to approximate the high even-order moments, and showed $\ln[\langle\Gamma_A^{2m}\rangle^{1/2m}/\langle\Gamma_A^{2m-2}\rangle^{1/(2m-2)}] \approx \ln[m/(m-1)] + \ln(4\pi m)/(4m) - \ln[4\pi(m-1)]/[4(m-1)]$ (see their equation 4), which is shown as solid lines in figure 7. As the order increases, our results approach the solid lines, and

https://doi.org/10.1017/jfm.2026.11481 Published online by Cambridge University Press

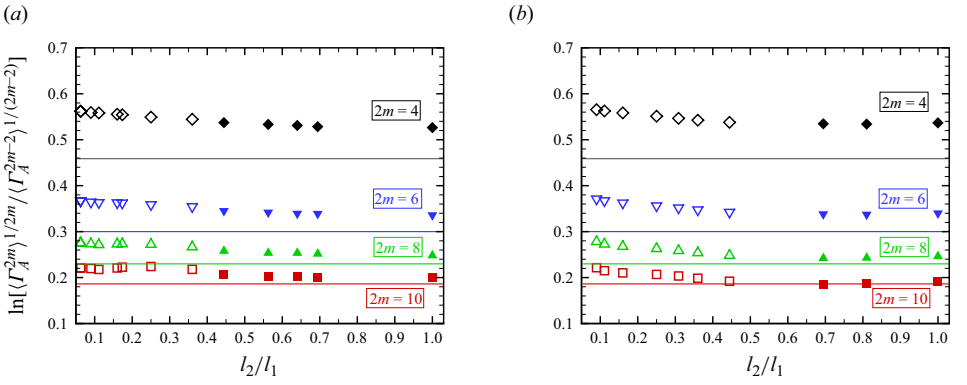


Figure 7. The logarithm of ratio of successive even-order circulation moments versus aspect ratio l_2/l_1 with a fixed area A: (*a*) $y^+ = 40$ at $A/\eta^2 \approx 26\,000$; (*b*) $y^+ = 0.3Re_\tau$ at $A/\eta^2 \approx 10\,000$. Filled symbols correspond to l_1 and l_2 both inside the inertial range, and hollow symbols correspond to the rectangles with at least one side outside the inertial range. The horizontal lines correspond to equation (4) of Iyer *et al.* (2021). Here, $Re_\tau = 2000$.

the agreement is quite good for $y^+ = 0.3Re_\tau$, agreeing with the observations of Iyer *et al.* (2021) in HIT and validating the area rule for the tails of the normalised circulation (Migdal 1994).

4. Conclusion

Exploring universal small-scale dynamics in turbulence is important, and two-point structure functions of velocity increments have shown that the universality in the inertial range is hindered by the intermittency. In the framework of Migdal (1994), recent attempts have demonstrated that velocity circulation, a quantity associated with the velocity increments via the Stokes theorem, displays a bifractal feature, much simpler than the multi-fractal characteristics in the velocity increments (Iyer *et al.* 2019; Müller *et al.* 2021; Polanco *et al.* 2021; Zhu *et al.* 2023). Importantly, the recent work of Duan *et al.* (2025) showed that the channel flow statistics of the area integral of the wall-normal vorticity component also exhibit bifractality, showing that this characteristic is not only the circumstance in ideal homogeneous turbulence but also in wall-bounded shear flow.

In this work, we demonstrate that this characteristic is also permitted in turbulent pipe flows, which have a curved wall, differing from the flat walls in channels. In cylindrical shells parallel to the pipe wall, we take the statistics of the velocity circulation, which equals to the area integral of the wall-normal vorticity via the Stokes theorem. The moments of the circulation show a bifractal singularity in the outer region, whereas they exhibit a unifractal non-singular behaviour in the inner region close to the wall. This makes for a close analogy with the statistics in channel flow, demonstrating that the geometric shape or azimuthal curvature in particular may not be a constraint factor to such statistics. The observed unifractality can be understood by examining how extreme events are suppressed. The viscous effects, which are strongest near the wall, suppress such extreme events, giving a more Gaussian PDF of the wall-normal vorticity. However, for the circulation with a small loop area, viscosity alone does not yield a fully Gaussian PDF. The remaining deviations from Gaussianity are progressively averaged out by integrating over a larger loop area (as evidenced from the kurtosis). In the inertial range, if the intermittency level is low, suppressed by the averaging effect, a unifractality is expected.

https://doi.org/10.1017/jfm.2026.11481 Published online by Cambridge University Press

In our work, we selected data in a cylindrical shell mainly to fulfil the homogeneity condition, following the former studies. The validity of the area rule over loops enclosing non-homogeneous flows is less studied. Nevertheless, an approximate area rule was reported also in planes that are not parallel to the wall in contracting geometries (Mugundhan & Thoroddsen 2023). Since such planes will contain flow structures that are not naturally homogeneous, Mugundhan & Thoroddsen (2023) finding suggests a broader generality of the area rule. Further studies with non-homogeneous flow data in other flow systems are needed to better evidence the generality.

Acknowledgements. D.X. would like to acknowledge Dr H. Li (Institute of Mechanics, Chinese Academy of Sciences) for insightful discussion. The authors also thank SuperComputing Network (SCNet) for providing the computing resources.

Funding. This work was supported by NSFC Excellence Research Group Program for 'Multiscale Problems in Nonlinear Mechanics' (No. 12588201), National Natural Science Foundation of China (Nos. 12372224, 92152106, 12322209 and 12272264) and Chinese Academy of Sciences (Project for Young Scientists in Basic Research, No. YSBR–087; Strategic Priority Research Program, No. XDB0620102).

Declaration of interests. The authors report no conflicts of interest.

Data availability statement. The data that support the findings of this study are available upon reasonable request to the corresponding author.

Author contributions. B.S.: performed simulation, wrote and reviewed the manuscript text. D.X.: conceptualised the study, analysed the data and prepared the figures and wrote and reviewed the manuscript.

References

Adrian, R.J. 2007 Hairpin vortex organization in wall turbulence. *Phys. Fluids* **19**, 041301.

Alhareth, A.A., Mugundhan, V., Langley, K.R. & Thoroddsen, S.T. 2024 Turbulent structure and circulation inside different planar contractions. *Phys. Fluids* **36**, 075129.

Apolinário, G.B., Moriconi, L., Pereira, R.M. & Valadão, V.J. 2020 Vortex gas modeling of turbulent circulation statistics. *Phys. Rev. E* **102**, 041102.

Avila, M., Willis, A.P. & Hof, B. 2010 On the transient nature of localized pipe flow turbulence. *J. Fluid Mech.* **646**, 127–136.

Benzi, R., Biferale, L., Struglia, M.V. & Tripiccione, R. 1997 Self-scaling properties of velocity circulation in shear flows. *Phys. Rev. E* **55**, 3739.

Cao, N., Chen, S. & Sreenivasan, K.R. 1996 Properties of velocity circulation in three-dimensional turbulence. *Phys. Rev. Lett.* **76**, 616.

Chen, K., Xu, D. & Song, B. 2022 Propagation speed of turbulent fronts in pipe flow at high Reynolds numbers. *J. Fluid Mech.* **935**, A11.

Duan, P.-Y., Chen, X. & Sreenivasan, K.R. 2025 Multiscale circulation in wall-parallel planes of turbulent channel flows. *J. Fluid Mech.* **1009**, R4.

Frisch, U. 1995 *Turbulence: The Legacy of A. N. Kolmogorov*. Cambridge University Press.

Iyer, K.P., Bharadwaj, S.S. & Sreenivasan, K.R. 2021 The area rule for circulation in three-dimensional turbulence. *Proc. Natl Acad. Sci.* **118**, e2114679118.

Iyer, K.P., Sreenivasan, K.R. & Yeung, P.K. 2019 Circulation in high Reynolds number isotropic turbulence is a Bifractal. *Phys. Rev. X* **9**, 041006.

Jodai, Y. & Elsinga, G.E. 2016 Experimental observation of hairpin auto-generation events in a turbulent boundary layer. *J. Fluid Mech.* **795**, 611–633.

Kolmogorov, A.N. 1941 The local structure of turbulence in incompressible viscous fluid for very large Reynolds numbers. *Dokl. Akad. Nauk SSSR* **30**, 299–303.

Marusic, I. & Monty, J.P. 2019 Attached eddy model of wall turbulence. *Annu. Rev. Fluid Mech.* **51**, 49–74.

Migdal, A.A. 1994 Loop equation and area law in turbulence. *Intl J. Mod. Phys. A* **09**, 1197.

Migdal, A.A. 1995 Loop equation and area law in turbulence. In *Quantum Field Theory and String Theory* (ed. L. Baulieu, V. Dotsenko, V. Kazakov & P. Windey). Springer.

Migdal, A.A. 2023 Statistical equilibrium of circulating fluids. *Phys. Rep.* **1011**, 1–117.

Moriconi, L. 2021 Multifractality breaking from bounded random measures. *Phys. Rev. E* **103**, 062137.

https://doi.org/10.1017/jfm.2026.11481 Published online by Cambridge University Press

MUGUNDHAN, V. & THORODDSEN, S.T. 2023 Circulation in turbulent flow through a contraction. *J. Turbul.* **24** (11-12), 577–612.

MÜLLER, N.P., POLANCO, J.I. & KRSTULOVIC, G. 2021 Intermittency of velocity circulation in quantum turbulence. *Phys. Rev. X* **11**, 011053.

POLANCO, J.I., MÜLLER, N.P. & KRSTULOVIC, G. 2021 Vortex clustering, polarisation and circulation intermittency in classical and quantum turbulence. *Nat. Commun.* **12**, 7090.

SHE, Z.-S. & LEVEQUE, E. 1994 Universal scaling laws in fully developed turbulence. *Phys. Rev. Lett.* **72**, 336–339.

SREENIVASAN, K.R., JUNEJA, A. & SURI, A.K. 1995 Scaling properties of circulation in moderate-Reynolds-number turbulent wakes. *Phys. Rev. Lett.* **75**, 433.

SREENIVASAN, K.R. & YAKHOT, V. 2021 Dynamics of three-dimensional turbulence from Navier–Stokes equations. *Phys. Rev. Fluids* **6**, 104604.

UMEKI, M. 1993 Probability distribution of velocity circulation in three-dimensional turbulence. *J. Phys. Soc. Japan* **62**, 3788.

WILLIS, A.P. 2017 The openpipeflow Navier–Stokes solver. *SoftwareX* **6**, 124–127.

WILLIS, A.P. & KERSWELL, R.R. 2009 Turbulent dynamics of pipe flow captured in a reduced model: puff relaminarization and localized edge states. *J. Fluid Mech.* **619**, 213–233.

WU, X. & MOIN, P. 2009 Direct numerical simulation of turbulence in a nominolly zero-pressure-gradient flat-plate boundary layer. *J. Fluid Mech.* **630**, 5–41.

XU, D. & AVILA, M. 2018 The effect of pulsation frequency on transition in pulsatile pipe flow. *J. Fluid Mech.* **857**, 937–951.

YAO, J., REZAEIRAVESH, S., SCHLATTER, P. & HUSSAIN, F. 2023 Direct numerical simulations of turbulent pipe flow up to $Re_\tau \approx 5200$. *J. Fluid Mech.* **956**, A18.

ZHOU, Q., SUN, C. & XIA, K.Q. 2008 Experimental investigation of homogeneity, isotropy, and circulation of the velocity field in buoyancy-driven turbulence. *J. Fluid Mech.* **598**, 361.

ZHU, H.-Y., XIE, J.-H. & XIA, K.-Q. 2023 Circulation in quasi-2D turbulence: experimental observation of the area rule and bifractality. *Phys. Rev. Lett.* **130**, 214001.

https://doi.org/10.1017/jfm.2026.11481 Published online by Cambridge University Press